

## **Sintering investigations of a UO<sub>2</sub>-PuO<sub>2</sub> powder synthesized using the freeze-granulation route**

Marion Le Guellec\*, Florent Lebreton\*, Laure Ramond\*, Abibatou Ndiaye‡,  
Thierry Gervais‡ & Guillaume Bernard-Granger\*

\*CEA, DES, ISEC, DMRC, Univ Montpellier, Marcoule France

‡ ORANO MELOX, Chusclan, France

### **Abstract**

Sintering investigations of a UO<sub>2</sub>-PuO<sub>2</sub> powder, integrating 11 wt% of PuO<sub>2</sub> and synthesized by freeze-granulation, were completed at temperatures up to 1700 °C, in an atmosphere of Ar/4 vol% H<sub>2</sub> and 1200 vpm H<sub>2</sub>O. Analyzing the “grain size versus relative density” trajectory enabled to propose that densification was controlled by volume diffusion and grain growth by the grain boundaries. An activation energy around 630 kJ/mol was obtained for densification, which was close to the value reported for volume diffusion of plutonium cations in U<sub>1-x</sub>Pu<sub>x</sub>O<sub>2</sub> polycrystals. The sintered microstructure appeared homogeneous regarding the plutonium and uranium cations distribution.

**Keywords:** Sintering; ceramics; oxides; microstructure; MOX

*The submitted paper is original and has not been or is not being submitted to  
the peer review process to any other journal*

\*Corresponding author: [guillaume.bernard-granger@cea.fr](mailto:guillaume.bernard-granger@cea.fr)

MOX fuels ( $\text{UO}_2\text{-PuO}_2$ ) are used in light water nuclear reactors and are potential candidates for fast neutron reactors. Industrial MOX pellets are manufactured by a dry-route process (grinding, pressing and sintering). Sintering at high temperature of MOX fuels was investigated in the past in function of the plutonium oxide content, in different kinds of atmospheres and sometimes using hot-pressing [1-6]. However the obtained results were not very conclusive in identifying the mechanisms controlling densification and microstructure development. Recently, the freeze-granulation route was shown to be a promising approach to manufacture MOX fuel pellets [7]. Highly flowable, dustless and easy-to-press MOX granules were elaborated [7]. Sintering of green compacts gives highly dense and defect-free pellets exhibiting a very homogeneous U-Pu spatial distribution [7]. The purpose of this paper is to rigorously investigate the sintering behavior of powder compacts made of such granules.

A homogeneous  $\text{UO}_2\text{-PuO}_2$  powder, containing 11 wt%  $\text{PuO}_2$  was prepared using the freeze-granulation route optimized by La Lumia [7]. The  $\text{UO}_2$  powder used was synthesized through a liquid route from uranyl nitrate solution. The  $\text{PuO}_2$  powder was obtained by oxalic precipitation of plutonium (IV) nitrate and calcination. Supplementary material shows the morphology of some individual granules observed using SEM (scanning electron microscopy, JCM-6000Plus, Jeol). They have a spherical shape and are devoid of any central cavity. Laser particle size distribution measured in dry mode (Mastersizer 3000, Malvern Panalytical, Mie configuration, air pressure fixed to 0.1 bar) is also shown in supplementary material. The volume distribution appears monomodal. The volume mean ( $D[4;3]$ ) and median ( $D_v(50)$ ) diameters are 915 and 775  $\mu\text{m}$ , respectively. The Pu/(U+Pu) content in the freeze-granulated powder was determined to be 10.5 at% using thermal ionization mass spectrometry (TIMS, VG-54 magnetic sector mass spectrometer, Isotopx).

Cylindrical samples (diameter of 5.4 mm and a height of 7 mm) were obtained by uniaxial pressing the freeze-granulated powder with a compaction pressure set to 450 MPa (manual hydraulic press, Atlas 25, Specac). By taking a theoretical volume mass of 11.034 g/cm<sup>3</sup> at room temperature, the relative green density was around 54-55 %.

The green pellets were sintered from room temperature to 1700 °C in a high temperature dilatometer (DIL402C, Setaram) under Ar/4 vol% H<sub>2</sub>. Dioxygen partial pressure of the atmosphere was monitored and controlled with an oxygen pump (Gen'air, Setnag) in order to have a water concentration of 1200 vpm during all the sintering runs (the oxygen partial pressure, calculated using the Wheeler approach [8], is fixed at 5.0x10<sup>-26</sup> bar at 650 °C, which gives 5.8x10<sup>-11</sup> bar at 1700 °C). Different heating rates: 2, 5 and 10 °C/min were used. All the runs have been completed using a heating rate fixed to 2 °C/min, from room temperature to 600 °C, in order to eliminate the organic compounds (dispersant and binder) used to elaborate the freeze-granulated powder. Because the mass of the samples does not change significantly between the green and fired states (small weight loss accounting for the organic compounds and adsorbed humidity present in the granules), the following relation is obtained [9-10]:

$$D_{(T)}(\%) = D_0 \frac{1}{\xi^2 \left[ 1 + \frac{\Delta L_{(T)}}{L_0} \right]^3} e^{3\alpha(T-T_0)} \quad (1)$$

where:  $D_{(T)}$  is defined as the sample instantaneous relative density,  $D_0$  is the relative green density,  $\xi$  is representative of the shrinkage anisotropy of the sample and is given by  $\xi = \frac{\phi_f L_0}{\phi_0 L_f} = \frac{\phi_{(T)} L_0}{\phi_0 L_{(T)}}$  with  $\phi_f$  the final diameter,  $L_f$  the final height,  $\phi_0$  the initial diameter,  $L_0$  the initial height,  $\phi_{(T)}$  the instantaneous diameter and  $L_{(T)}$  the instantaneous height,  $\Delta L_{(T)} = L_{(T)} - L_0$  ( $<0$ ) is the sample height variation,  $\alpha$  is the linear thermal expansion coefficient,  $T$  is the instantaneous temperature and  $T_0$  the room temperature. From a practical point

of view,  $\alpha$  is determined from the cooling steps of the dilatometer runs. An average value of  $12.1 \times 10^{-6} \pm 1.3 \times 10^{-6} / ^\circ\text{C}$  is retained. All the sintering tests carried out have shown that the parameter  $\xi$  is close to 1.

Fig. 1a shows how the relative density is progressing in function of temperature. Whatever the heating rate, samples start to densify around 650 °C. The lower the heating rate, the higher the relative density for a given temperature. Such a behavior is well known and was previously observed for numerous non-radioactive oxides as zirconia, alumina and spinel [9-12]. As proposed by Sato, the lower the heating rate, the longer the exposure time above the sintering onset temperature and the higher the shrinkage and relative density reached at a given temperature [11]. Fig. 1b shows the variation of the instantaneous densification rate as a function of temperature. The higher the heating rate, the higher the instantaneous densification rate whatever the temperature. This trend is also well known and was previously reported for non-radioactive oxides [9-10, 13]. It has also to be outlined that the higher the heating rate, the higher the temperature of the maximum in densification rate: 1421 °C for 2 °C/min, 1461 °C for 5 °C/min and 1547 °C for 10 °C/min. Fig. 1c is a zoom of Fig. 1b in the 600-1200 °C temperature range. Whatever the heating rate (and even if it is more delicate to observe for the lowest heating rate), the instantaneous densification rate exhibits a first maximum value around 830 °C. It means that densification starts around 650 °C and slows-down from 830 °C. Similar results were reported by several authors investigating the sintering behavior in different kinds of atmospheres of  $\text{UO}_2$ -20 wt%  $\text{PuO}_2$  [1],  $\text{UO}_2$ -30 wt%  $\text{PuO}_2$  [14] fuels and  $\text{UO}_2$ -30 wt%  $\text{CeO}_2$  surrogates [15]. For them, the densification slow-down correlates with the onset of a  $\text{UO}_2$ - $\text{PuO}_2$  or  $\text{UO}_2$ - $\text{CeO}_2$  solid solution formation. Even if additional experiments are required, we postulate that a solid solution forms in the densifying samples around 830 °C, whatever the heating rate used. Because the solid solution is formed by the interdiffusion of  $\text{Pu}^{4+}$  cations into  $\text{UO}_2$  lattice and  $\text{U}^{4+}$  cations into  $\text{PuO}_2$  lattice it decreases the densification rate temporarily until

completion and then densification restarts with a polycrystalline sample made of  $U_{1-x}Pu_xO_{2\pm x}$  grains. Accordingly, when densification resumes around 950-1050°C, the samples are more homogeneous and can be described as a polycrystalline body constituted by pores and grains of  $U_{1-x}Pu_xO_{2\pm x}$  solid solutions, rather than  $UO_2$  and  $PuO_2$  grains. We are aware that the previous hypothesis needs to be corroborated in the future using, for example, X-ray diffraction (XRD) experiments at high temperature and interrupted sintering tests around 830 °C followed by careful microstructure characterizations. Indeed, other reasons may lead to a maximum in the densification rate for low temperatures, as for example stepwise particle rearrangement at early sintering offset. Interesting is also the tendency given by Fig. 1d showing the variation of the absolute instantaneous densification rate in function of  $D(T)$ . All curves exhibit a maximum value around  $1.2 \times 10^{-5}$  /K when the instantaneous relative density is in the range 67-70%, which corresponds more or less to the end of the step related to the necks formation between the elemental crystallites and/or the individual freeze-dried granules. In addition, the three curves overlap. This means that the densification mechanism is the same for the three heating rates used.

Figs. 2a, 2b and 2c show some examples of the sintered microstructure, observed using SEM (Supra 55 VP, Zeiss), for samples having a relative density of 82.8, 89.2 and 96.9% (Archimedes method with immersion in bromobenzene), respectively, and obtained under different thermal conditions. Samples having a relative density below 90% (transition between an open and closed porosity) exhibit an intergranular fracture surface (Figs. 2a and 2b). Conversely, samples with a relative density above 90% give an intragranular fracture surface (Fig. 2c). For samples giving an intergranular fracture, as is also the case for green compacts, it is easy to determine the average grain size by the intercept method (at least 300 grains are considered, correction factor set to 1.56 even if such a value is usually used for planar surfaces which is not strictly the case of a

fracture surface) [16]. For samples with an intragranular fracture, the grain size is only approximated by finding zones where the elementary grains are observed unequivocally (around 40 grains only, same correction factor). Knowing the relative density and the grain size of each sintered sample, it is possible to construct the “grain size versus relative density” trajectory named the “sintering path”, as shown on Fig. 2d. The experimental points belong to a single trajectory (dashed curve on Fig. 2d), independent of sintering temperature, soak time and heating rate. Accordingly, the grain size can be described as a monotonous function of the relative density and a multitude of sintering experimental conditions led to the same microstructure, as was previously reported for other non-radioactive oxides [9-10, 13]. From Fig. 2d, it also appears that grain growth is moderate when the relative density is lower than 90% and is on contrary pronounced above.

XRD (D8 Advance, Bruker, equipped with a Lynx Eye detector and a Cu-K $\alpha$ /K $\beta$  source with  $\lambda_{K\alpha/K\beta} = 154.06/154.44$  pm) experiments were carried out on the sample sintered at 1700 °C for 4 h (heating rate fixed to 2 °C/min, relative density is 96.9% and grain size around 14  $\mu$ m). A single phase is detected, having the fluorite structure (Fm $\bar{3}$ m, space group 225) and a lattice parameter of 546.25 pm (Le Bail analysis using FullProf Suite). The Pu/(U+Pu) content has been determined to be 10.5 at% using TIMS (same value as in granules). Philipponneau proposed a relationship linking the lattice parameter,  $a$ , to the Pu/(U+Pu) content,  $y$ , and the deviation from stoichiometry,  $x$ , for U $_{1-y}$ Pu $_y$ O $_{2-x}$  solid solutions [17]:

$$a(pm) = 547 - 7.4y + 32x \quad (2)$$

According to relation (2) we obtain a  $x$  value close to  $1 \times 10^{-3}$ . Thus the average composition of the sintered polycrystal is U $_{0.895}$ Pu $_{0.105}$ O $_{1.999}$ . The O/M value is

almost 2, which is compatible to the one required for MOX fuels dedicated to nuclear light water reactors.

All the experimental points constituting the sintering path shown on Fig. 2d were fitted with theoretical expressions linking the grain size to the relative density [18]. The best determination coefficient value amongst these fits is obtained when grain growth is controlled by the grain boundaries and densification is controlled by volume diffusion (see fit on Fig. 3a).

Let us now determine the apparent activation energy for the mechanism controlling densification supposed to be volume diffusion. The equation for the densification rate can be separated into temperature-dependent, grain size-dependent, density-dependent quantities and rearranged as follows [10, 12, 19]:

$$\text{Ln} \left[ T \frac{dD}{dT} \frac{dT}{dt} \right] = - \frac{Q_d}{RT} + \text{Ln}\{F[D]\} + \text{Ln}(A) - n\text{Ln}(G) \quad (3)$$

where  $A$  is a constant,  $F[D]$  is a function only of density,  $Q_d$  is the apparent activation energy for the mechanism controlling densification,  $R$  is the universal gas constant,  $T$  is the absolute temperature,  $G$  is the grain size,  $n$  is the grain size exponent whose value depends on whether the densification rate is controlled by lattice diffusion ( $n = 3$ ) or grain-boundary diffusion ( $n = 4$ ) and  $\zeta = dT/dt$  is the heating rate that is held constant during anisothermal sintering experiments.

A plot of the left-hand side of relation (3) versus  $1/T$  would give a value for  $Q_d$  provided that the data points are taken at a constant value of  $D$  and  $G$ . Fig. 2d displays that each value of relative density corresponds to a single value of grain size, regardless of the sintering conditions. Then, points for a constant value of  $D$  are generated by changing the heating rate. The measurements led to values of  $Q_d$  at different values of  $D$ . This formalism is known as the CRH method (Constant Rates of Heating). Using such an approach leads to Fig. 3b and an

almost constant apparent activation energy of  $635 \pm 25$  kJ/mol is calculated for the mechanism controlling densification.

A second method to determine the apparent activation energy for the mechanism controlling densification is to construct the Master Sintering Curve (MSC). By extending the analysis of sintering beyond the confined segments described by the individual stage models [20-21], it was shown, for isotropic shrinkage (true for the freeze-granulated powder investigated) and if there exists only one dominant diffusion mechanism (either volume or grain boundary diffusion), that [20]:

$$\frac{R}{3\gamma_{sv}\Omega\Phi_0} \int_{D_0}^D \frac{(G[D])^n}{D\Gamma[D]} dD = \int_0^t \frac{e^{-\frac{Q_d}{RT}}}{T} dt = \Theta_d(h/K) = \frac{1}{\zeta} \int_{T_0}^T \frac{e^{-\frac{Q_d}{RT}}}{T} dT \quad (4)$$

where  $\gamma_{sv}$  is the solid/vapor surface tension,  $\Phi_0 = \Phi_{v0}$  and  $n = 3$  for volume diffusion,  $\Phi_0 = \delta_b\Phi_{b0}$  with  $\delta_b$  the grain boundary thickness and  $n = 4$  for grain boundary diffusion ( $\Phi_0$  is the pre-exponential factor of the diffusion coefficient),  $\Gamma[D]$  and  $G[D]$  (the grain size) are functions only of the relative density,  $T_0$  is the temperature at which densification is effectively starting (assumed to be 1000 °C at the end of solid solution formation) and the other parameters have been described previously. Because the left-hand site of Equation (4) is a function only of relative density, the MSC is simply defined as the relationship between the relative density  $D$  and  $\Theta_d$  [20]. To construct the MSC curve under anisothermal sintering conditions, we used the results from the dilatometer runs, the trapezoidal approximation and a curve-fitting procedure to determine the value of  $Q_d$  by minimizing the residual sum of squares (RSS) between the experimental and calculated values, assuming that all points must line up to form a single curve. Such an analysis leads to the results shown in Figs. 3c and 3d. The apparent activation energy for the mechanism controlling densification is then calculated to be around 600 kJ/mol.



Thereby, an average apparent activation energy equal to  $630 \pm 25$  kJ/mol, associated with the densification mechanism, is therefore determined from the CRH and MSC methods (average value and standard deviation calculated by taking into account the five values obtained from the CRH method and the single value calculated from the MSC analysis). Tab. 1 summarizes the volume diffusion coefficients and corresponding activation energies for uranium/plutonium cations and oxygen anions for  $U_{1-y}Pu_yO_{2\pm x}$  [22-25]. Plutonium cations are the slowest species and the activation energies measured by Noyau [24] and Lamb [25] are very close to the one measured during our sintering experiments. Accordingly, we postulate that volume diffusion of plutonium cations is controlling densification of the freeze-granulated powder investigated.

Finally, a polished cross section from the sample sintered for 4 h at 1700 °C (heating rate fixed to 2 °C/min) was characterized using electron probe microanalysis (SX100, Cameca). Measurements performed at 20 kV at the  $U-M_{\alpha}$  and  $Pu-M_{\beta}$  lines allowed the U-Pu distribution to be assessed and the Pu content was quantified by applying the ZAF method and using  $UO_2$  and  $PuO_2$  samples as standards for U, Pu and O. The resulting chemical mapping in Fig. 4 shows that the Pu repartition inside the pellet is very homogeneous, notably compared to pellets produced by conventional powder metallurgy processes [26-27]. MOX fuels with a very homogeneous U/Pu distribution are thought to have a better behavior under irradiation in reactors by preventing the formation of the high burnup structure [28-29].

**Acknowledgements:** The authors warmly thank Gauthier Jouan, Romain Lauwerier, Romain Vauchy and Patrice Signoret for their precious help during the experiments carried out within the framework of this study.

### **References**

- [1] T.R.G. Kutty, P.V. Hegde, K.B. Khan, S. Majumdar, D.S.C. Purushotham.  
J. Nucl. Mater. 282 (2000) 54-65
  
- [2] S. Noyau, F. Audubert, P.M. Martin, A. Maitre. J. Eur. Ceram. Soc. 35  
(2011) 3651-3663
  
- [3] S. Berzati, S. Vaudez, R.C. Belin, J. L  chelle, Y. Marc, J.C. Richaud, J.M.  
Heintz. J. Nucl. Mater. 447 (2014) 115-124
  
- [4] T.R.G. Kutty, P.V. Hegde, R. Keswani, K.B. Khan, S. Majumdar, D.S.C.  
Purushotham. J. Nucl. Mater 264 (1999) 10-19
  
- [5] S. Vaudez, J. L  chelle, S. Berzati, J.M. Heintz. J. Nucl. Mater. 460 (2015)  
221-225
  
- [6] J.L. Routbort, J.C. Voglewede, D.S. Wilkinson. J. Nucl. Mater. 80 (1979)  
348
  
- [7] F. La Lumia, L. Ramond, C. Pagnoux, P. Coste, F. Lebreton, J.R. Sevilla, G.  
Bernard-Granger. J. Amer. Ceram. Soc. 103 (2020) 3020-3029
  
- [8] V. J. Wheeler, I.G. Jones. J. Nucl. Mater. 42 (1972) 117-121
  
- [9] G. Bernard-Granger, C. Guizard. J. Amer. Ceram. Soc. 90 (2007) 1246-1250
  
- [10] N. Benameur, G. Bernard-Granger, A. Addad, S. Raffy, C. Guizard. J.  
Amer. Ceram. Soc. 94 (2011) 1388-1396

- [11] E. Sato, C.P. Carry, J. Amer. Ceram. Soc. 79 (1996) 2156-2160
  
- [12] J. Wang, R. Raj. J. Amer. Ceram. Soc. 73 (1990) 1172-75
  
- [13] G. Bernard-Granger, C. Guizard, A. Addad. J. Mater. Sci. 42 (2007) 6316-6324
  
- [14] R. Manzel, W.D. Dorr. Bull. Am. Ceram. Soc. 59 (1980)601-616
  
- [15] W. Dorr, S. Hellmann, G. Mages. J. Nucl. Mater. 140(1986) 7-10
  
- [16] M.I. Mendleson. J. Amer. Ceram. Soc. 52 (1969) 443-446
  
- [17] R. Vauchy, A.C. Robisson, R.C. Belin, P.M. Martin, A.C. Scheinost, F. Hodaj. J. Nucl. Mater. 465 (2015) 349-357
  
- [18] G. Bernard-Granger, C. Guizard. Acta Mater. 56 (2008) 6273–6282
  
- [19] J. Wang, R. Raj. J. Am. Ceram. Soc.74 (1991) 1959–63
  
- [20] J.D. Hansen, R.P. Rusin, M.H. Teng, D.L. Johnson. J. Am. Ceram. Soc. 75 (1992) 1129–35
  
- [21] H. Su, D.L. Johnson. J. Am. Ceram. Soc. 79 (1996) 3211–7
  
- [22] R. Vauchy, A.C. Robisson, P. Bienvenu. I. Roure, F. Hodaj, P. Garcia. J. Nucl. Mater. 467 (2015) 886-893
  
- [23] D.B. Knorr, R.M. Cannon, R.L. Coble. Acta Metall. 37 (1989) 2103-2123

- [24] S. Noyau. PhD Thesis, University of Limoges, (2012)
  
- [25] R.A. Lambert. PhD Thesis, University of Surrey, (1978)
  
- [26] T. Gervais, D. Favet, L. Paret, S. Vaudez. Proceedings of the International Conference on Fast Reactors and Related Fuel Cycles: Next Generation Nuclear Systems for Sustainable Developments, Yekaterinburg, (2017)
  
- [27] G. Oudinet, I. Munoz-Viallard, L. Afore, M.J. Gotta, J.M. Becker, G. Chiarelli, R.Castelli. J. Nucl. Mat. 375 (2007) 86-94
  
- [28] J. Noirot, L. Desgranges, J. Lamontagne. J. Nucl. Mater. 372 (2008) 318-339
  
- [29]. J. Noirot, Y. Pontillon, J. Lamontagne, I. Zacharie-Aubrun, K. Hanifi, P. Bienvenu, L. Desgranges. EPJ Web of Conferences 115 (2016) 04005

### **Figure captions**

Fig. 1: a) Relative density in function of temperature; b) Densification rate in function of temperature; c) zoom of b) in the 600-1200 °C temperature range; d) Absolute densification rate in function of temperature.

Fig. 2: a) Microstructure of the sample sintered to 82.8% relative density; b) Microstructure of the sample sintered to 89.2% relative density; c) Microstructure of the sample sintered to 96.9% relative density; d) Sintering path.

Fig. 3: a) Fitting of the experimental points for a scenario based on densification being controlled by volume diffusion and grain growth by the grain boundaries; b) Determination of the apparent activation energy for densification using the anisothermal CRH method; c) Determination of the apparent activation energy for densification using the anisothermal MSC method – Residual sum of squares, d) Determination of the apparent activation energy for densification using the anisothermal MSC method – MSC curve

Fig. 4: (A) Electron microprobe U-M<sub>α</sub> intensity mapping; b) Electron probe Pu-M<sub>β</sub> intensity mapping; c) colored pseudo-quantified Pu mapping.

Supplementary material: a) SEM observations of freeze-granulated granules; b) An individual broken granule observed by SEM showing the lack of central cavity; c) Volume fraction and cumulative volume fraction distributions from laser granulometer tests in dry mode on the freeze-granulated powder; d) Key parameters extracted from the volume distribution.

Fig.1

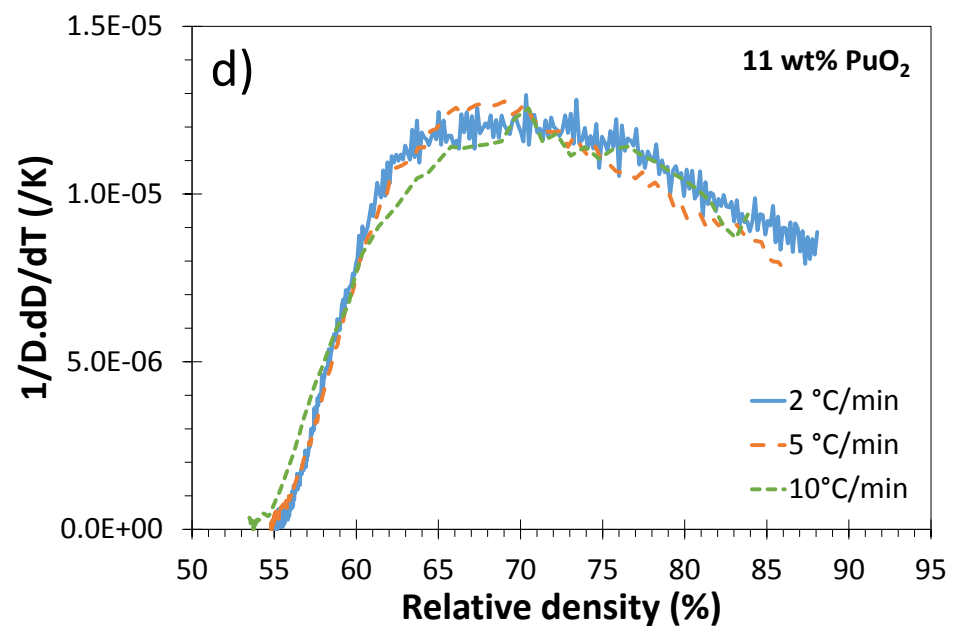
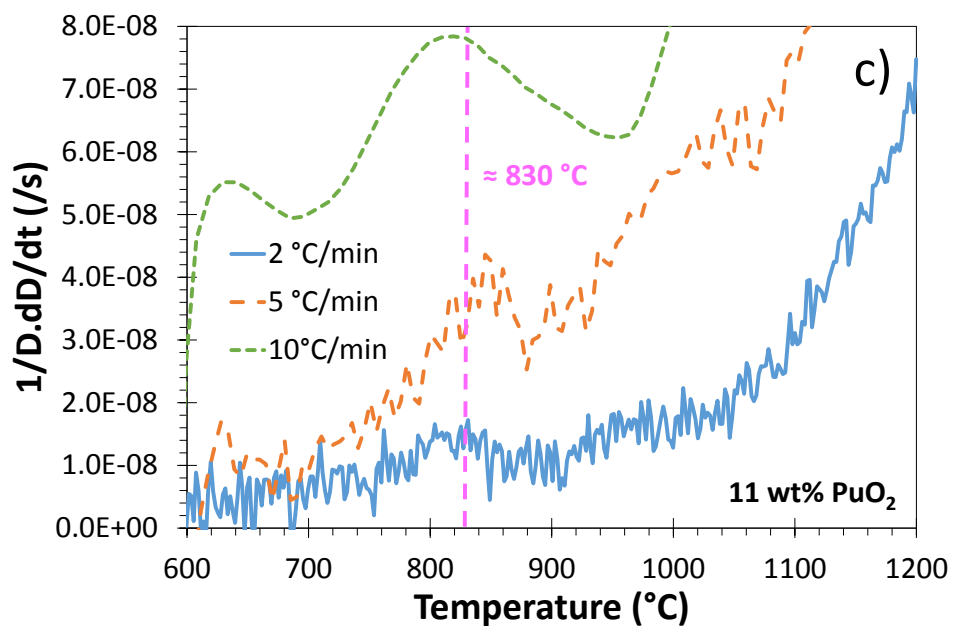
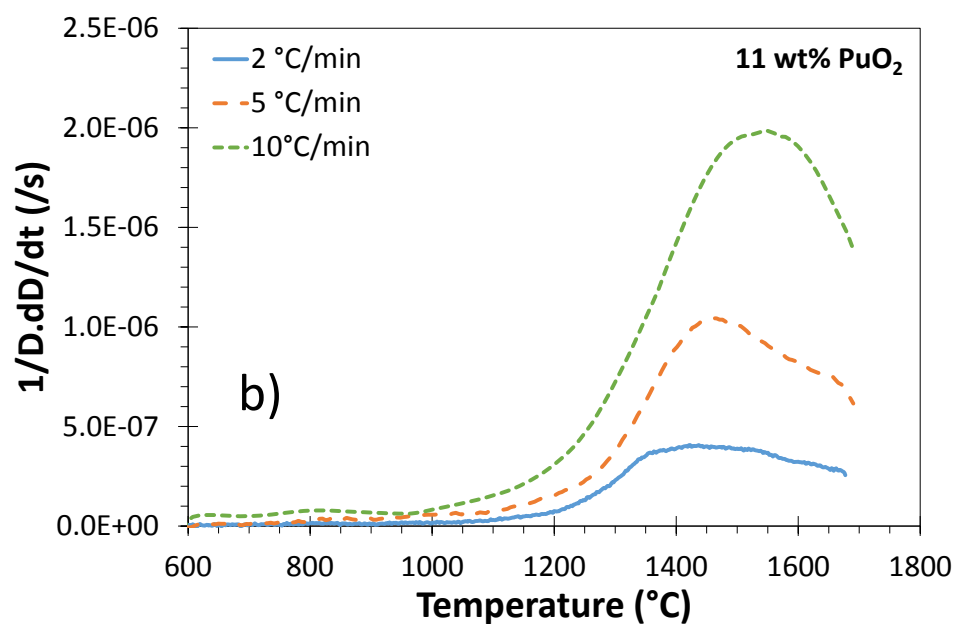
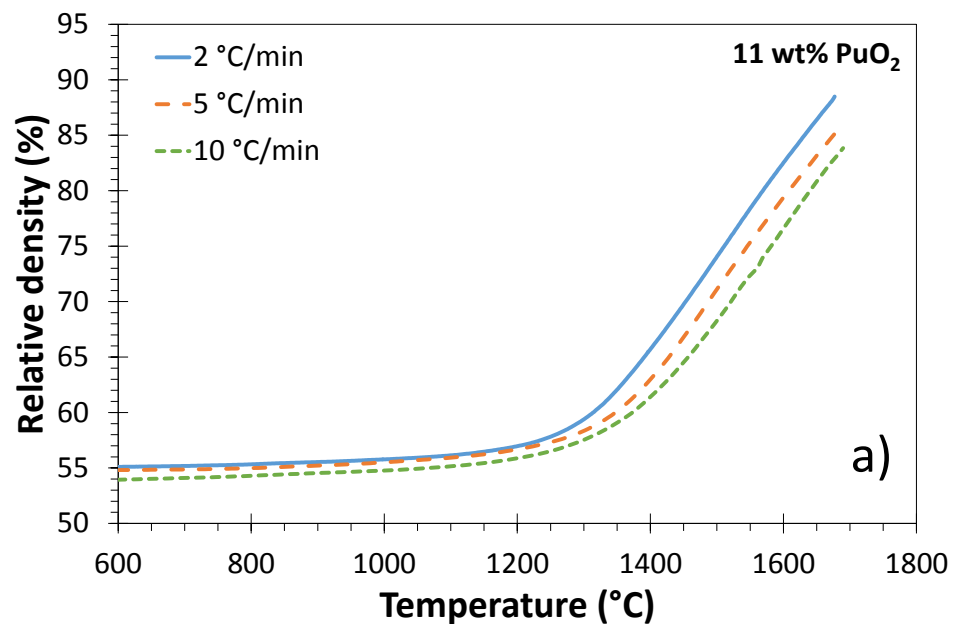
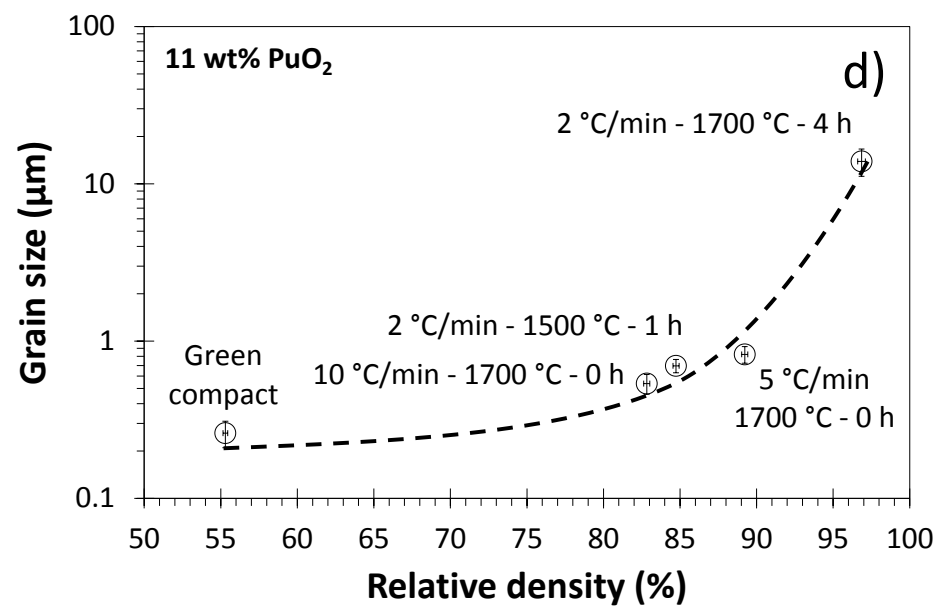
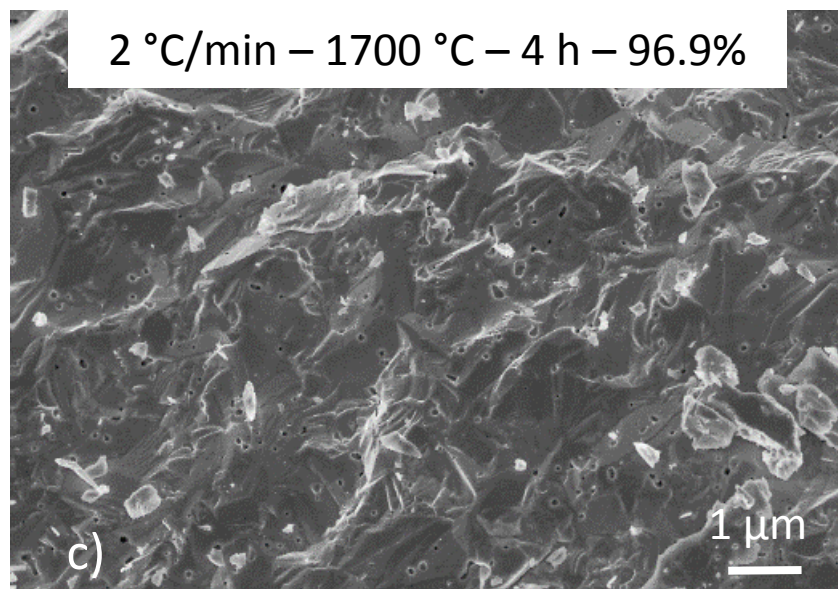
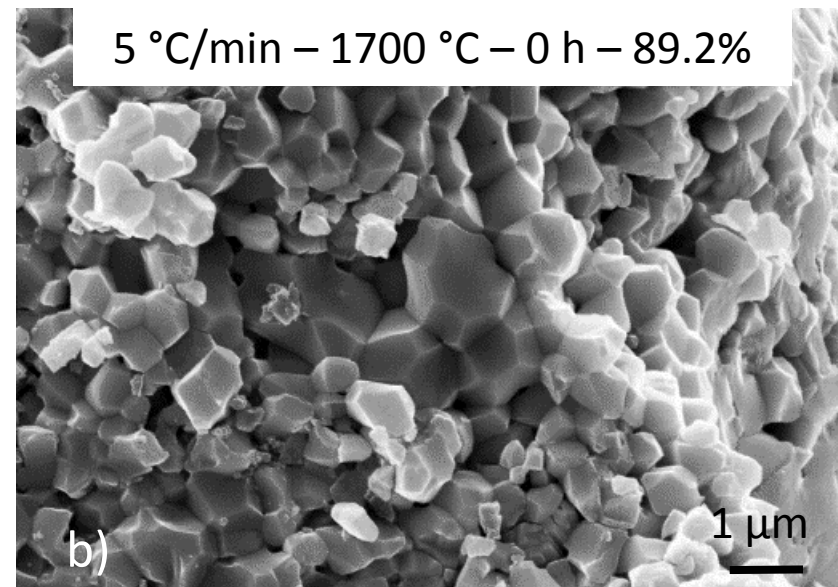
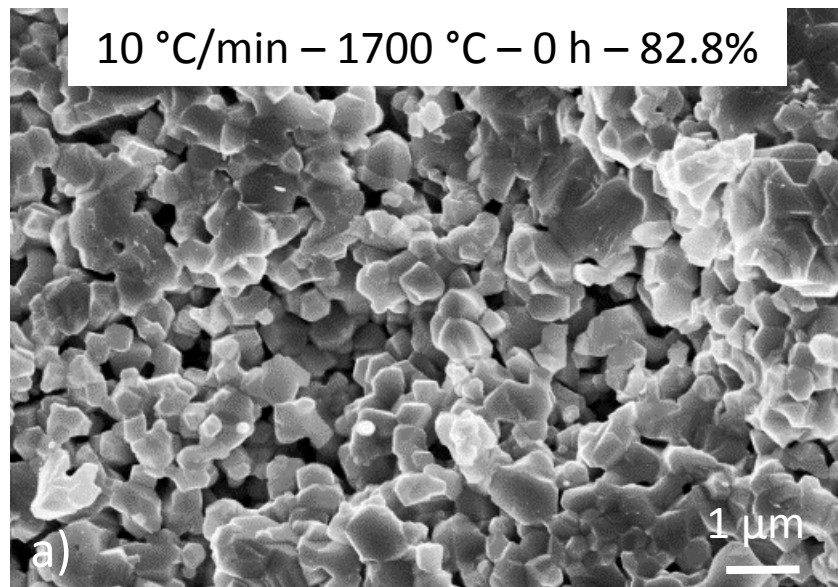


Fig.2



**Fig.3**

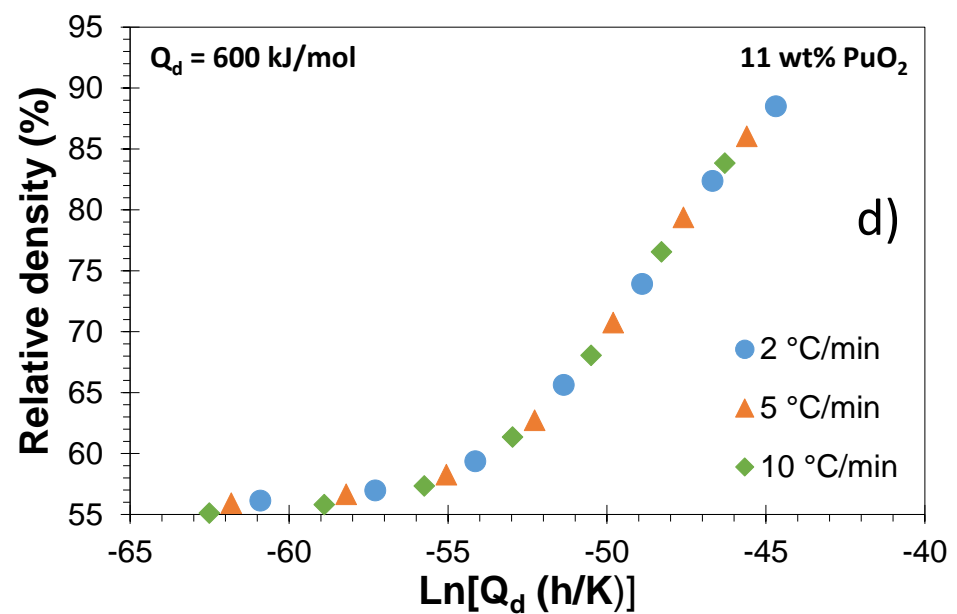
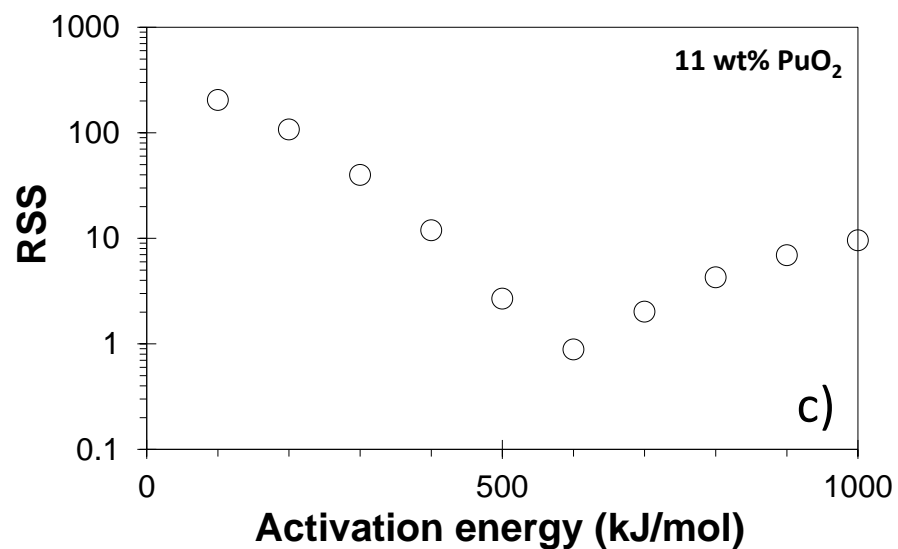
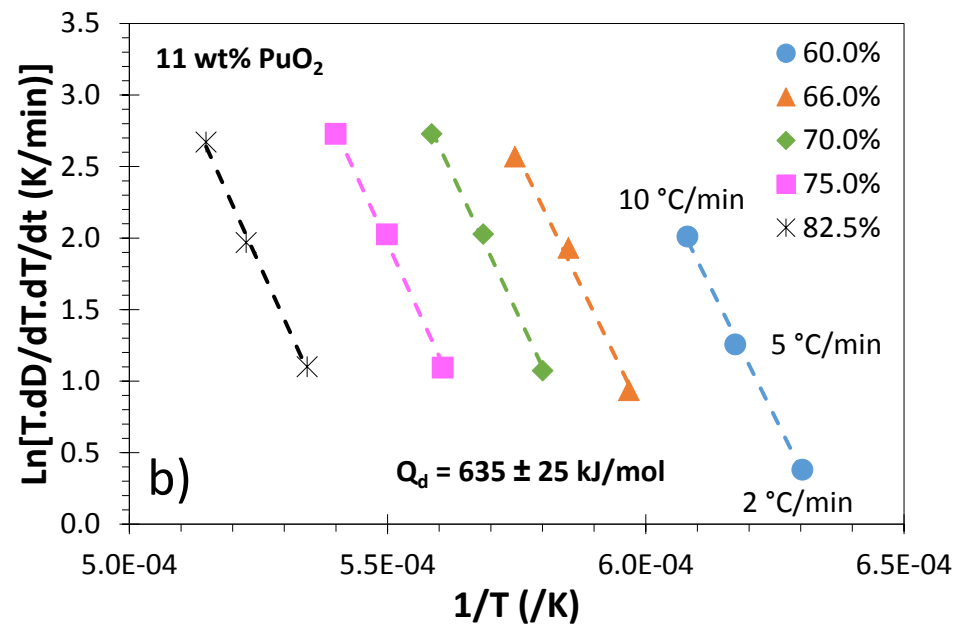
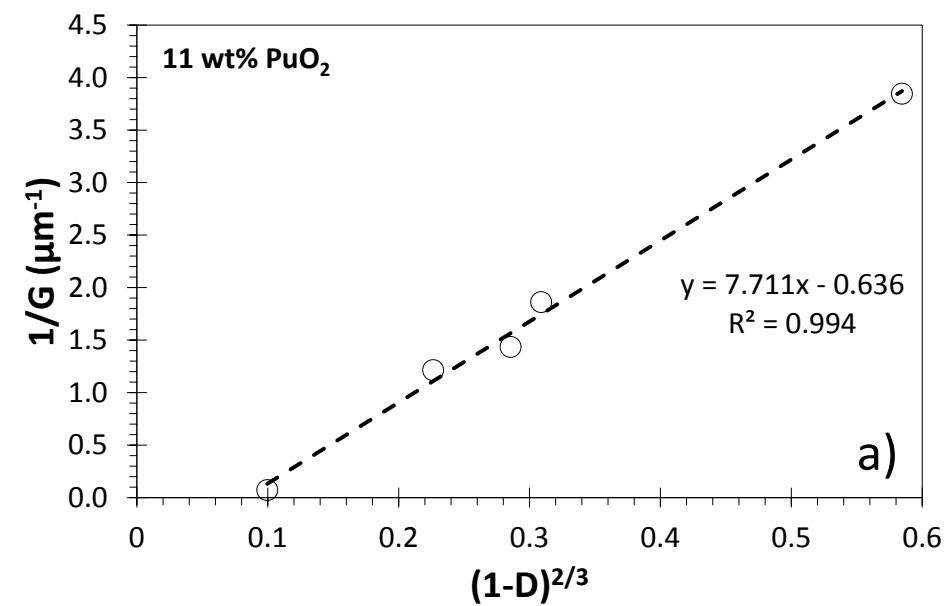
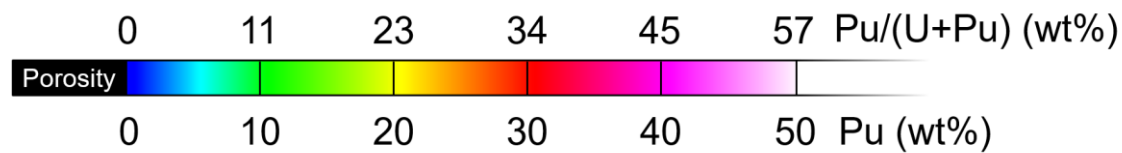
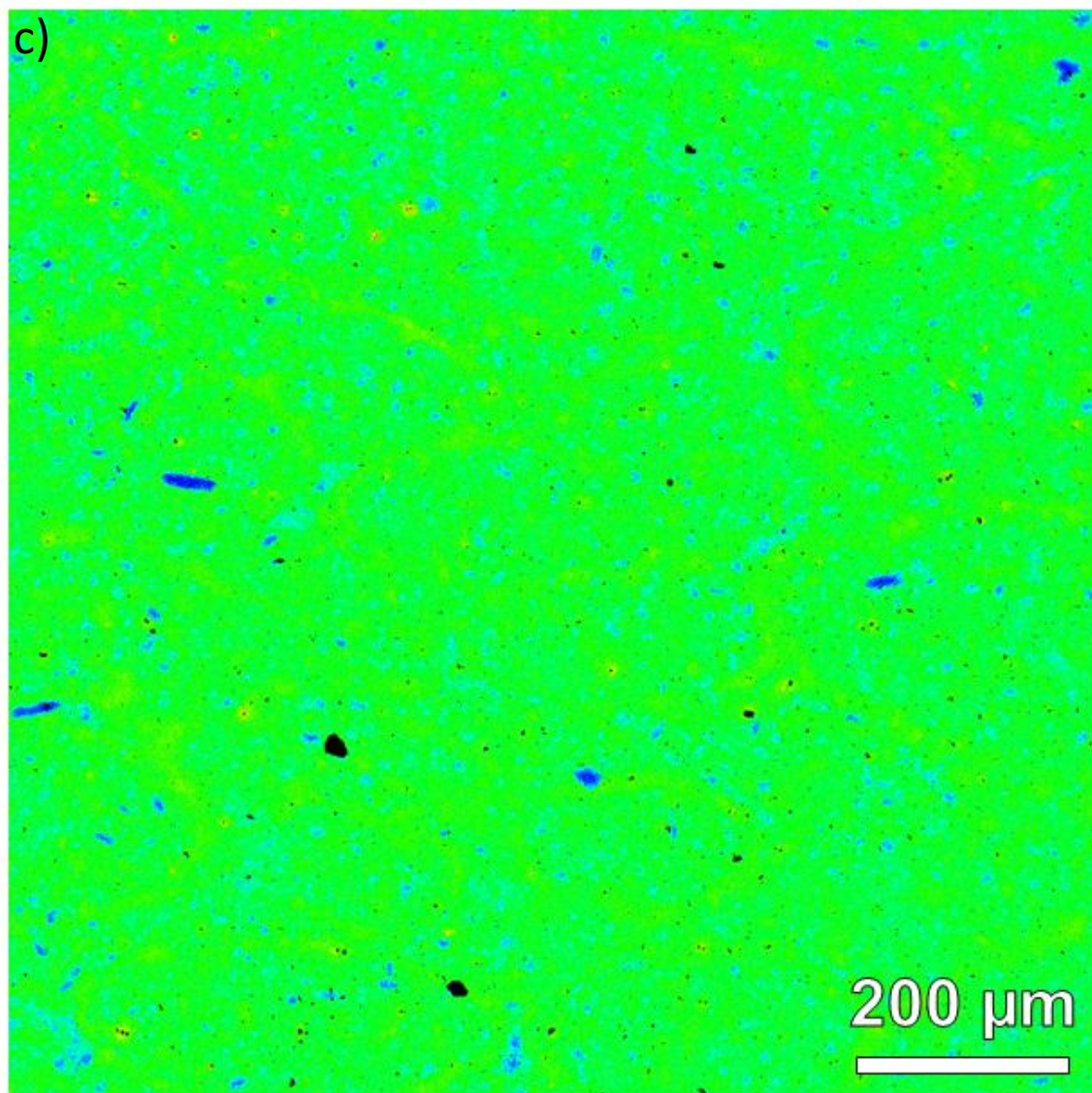
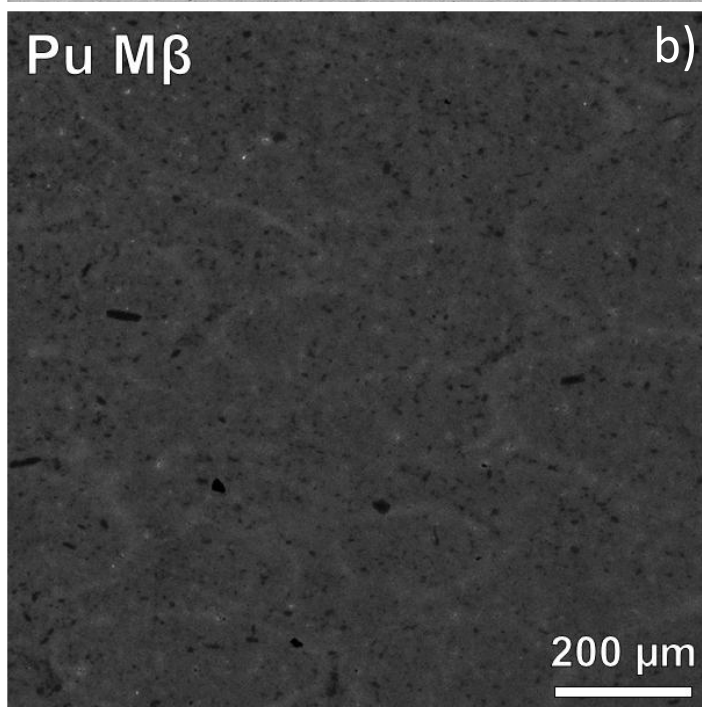
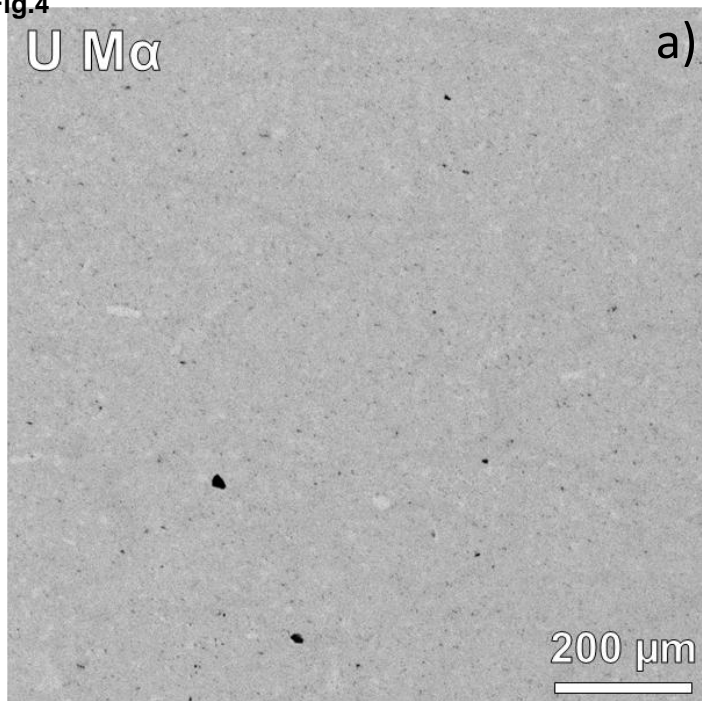




Fig.4



Tab.1

Species	Matrix	Temperature (°C)	Diffusion coefficient (m²/s)	Activation energy (kJ/mol)	Reference
O <sup>2-</sup>	U <sub>0.55</sub> Pu <sub>0.45</sub> O <sub>2</sub> Self-diffusion Polycrystal (35 μm)	800	1.5x10 <sup>-16</sup>	315	[22]
		1000	3.7x10 <sup>-14</sup>		
U <sup>4+</sup>	UO <sub>2</sub> Volume diffusion Best fits	1000	9.4x10 <sup>-28</sup>	545	[23]
		1200	1.0x10 <sup>-24</sup>		
		1400	2.0x10 <sup>-22</sup>		
		1500	1.8x10 <sup>-21</sup>		
		1600	1.3x10 <sup>-20</sup>		
Pu <sup>4+</sup>	U <sub>0.55</sub> Pu <sub>0.45</sub> O <sub>2</sub> Volume diffusion Polycrystal (10 μm)	1000	2.9x10 <sup>-29</sup>	625	[24]
		1200	8.5x10 <sup>-26</sup>		
		1400	3.7x10 <sup>-23</sup>		
		1500	4.7x10 <sup>-22</sup>		
		1600	4.5x10 <sup>-21</sup>		
Pu <sup>4+</sup>	U <sub>0.80</sub> Pu <sub>0.20</sub> O <sub>1.996</sub> Volume diffusion Monocrystal	1500	1.0x10 <sup>-21</sup>	636	[25]
		1600	1.0x10 <sup>-20</sup>		